4-2016

The effect of confinement on the development of an axisymmetric wall jet in confined jet impingement

Tianqi Guo

Graduate School Form
30 Updated 12/26/2015

PURDUE UNIVERSITY
GRADUATE SCHOOL
Thesis/Dissertation Acceptance

This is to certify that the thesis/dissertation prepared

By Tianqi Guo

Entitled

THE EFFECT OF CONFINEMENT ON THE DEVELOPMENT OF AN AXISYMMETRIC WALL JET IN CONFINED JET IMPINGEMENT

For the degree of Master of Science in Mechanical Engineering

Is approved by the final examining committee:

Pavlos P. Vlachos Chair	Jun Chen
Justin Weibel	

To the best of my knowledge and as understood by the student in the Thesis/Dissertation Agreement, Publication Delay, and Certification Disclaimer (Graduate School Form 32), this thesis/dissertation adheres to the provisions of Purdue University's "Policy of Integrity in Research" and the use of copyright material.

Approved by Major Professor(s): Pavlos P. Vlachos

Approved by: Jay P. Gore 4/26/2016

Head of the Departmental Graduate Program Date

THE EFFECT OF CONFINEMENT ON THE DEVELOPMENT OF AN AXISYMMETRIC WALL JET IN CONFINED JET IMPINGEMENT

A Thesis

Submitted to the Faculty

of

Purdue University

by

Tianqi Guo

In Partial Fulfillment of the

Requirements for the Degree

of

Master of Science in Mechanical Engineering

May 2016

Purdue University

West Lafayette, Indiana

To My Parents

ACKNOWLEDGEMENTS

I would like to express my sincere gratitude to my advisor, Professor Pavlos Vlachos, for his support and encouragement. His guidance was immensely significant for my personal growth over the past three years and would certainly guide my future career in the coming future. Also, I would like to extend my thanks to my graduate advisory committee, Professor Jun Chen and Professor Justin Weibel for their academic advice.

My special gratitude goes to Dr. Matthew Rau for his patient help and discussion during the experiment and data analysis. His hardworking and endeavors in academics will always be my example to follow. I also want to thank all my labmates, for keeping AEThER an extraordinary place to perform productive work. Last but not the least, my parents are always my crutch when my legs stop moving forward.

TABLE OF CONTENTS

Page

LIST OF FIGURES

Figure Page

LIST OF TABLES

Table Page

NOMENCLATURE

D	confinement plate diameter
d	jet orifice diameter
dz	translation before camera calibration
H	confinement height
L	nozzle-to-plate spacing
l_c	jet core length
$l_{crit,\alpha}$	critical distance of velocity decay
$l_{crit,\beta}$	critical distance of half-width growth
O	stagnation point, origin
Δt	time delay between laser pulses
u	x-component/radial velocity
u_m	local maximum of u velocity
u_{crit}	critical local maximum u
v	y-component/vertical velocity
V_j	jet exit velocity
$\|V\|$	velocity magnitude
w	z-component/out-of-plane velocity
x	horizontal directional vector
y	vertical directional vector
$Y_{1/2,i}$	measured wall jet half-width

$y_{1/2,i}$ nominal (fitted) wall jet half-width

z out-of-plane directional vector

Greek symbols

α decay rate of um

β_i growth rate of Y1/2, i

λ_{ci} swirling strength of a vortex

ν kinematic viscosity of water

ρ density of water

Subscript

i wall jet layer indicator

T Top layer

W Wall layer

ABSTRACT

Guo, Tianqi. M.S.M.E., Purdue University, May 2016. The Effect of Confinement on the Development of an Axisymmetric Wall Jet in Confined Jet Impingement. Major Professor: Pavlos P. Vlachos.

Impinging jets have been widely used in the industry for cooling, heating, drying and many other purposes due to their excellent level of mass and heat transfer capacities. When issued into a confinement gap fully filled with working liquid, which is a typical configuration for the compact cooling devices designed to handle the extremely high heat fluxes generated by continuously working electronic components, they are classified as submerged confined impingement jets. Though the complicated flow field induced by the jet has attracted enormous amount of research efforts from heat transfer as well as fluid dynamics points of view, many key questions still remain unanswered. The present work reports a detailed experimental study of the flow field surrounding an axisymmetric, confined, impingement jet using stereo particle image velocimetry (SPIV). The experiments are conducted at three different orifice-to-plate spacings (2, 4 and 8 jet diameters) across Reynolds number ranging from 1000 to 9000. A maximum spatial resolution of 25 μm is achieved and the temporal resolution of the measurement remains 750 Hz. Special attention has been paid to the development of the triple-layered wall-jet with incomplete self-similarity. The jet core length and expansion angle for the vertical

impingement jet has been calculated and presented. At small confinement height, the recirculating vortical structure has been found to strongly affect the wall-jet development. These flow field measurements and analysis will serve to inform a variety of practical applications in which impinging jets are used.

CHAPTER 1. EFFECT OF THE CONFINEMENT ON THE FLOW FIELD

1.1 Flow Field Characteristics

Impinging jets are ubiquitous in many engineering applications. Jets are used for cooling the leading edge of gas turbines (Han, 2004), rapid processing of foods (Sarkar et al., 2004), quenching of metal parts (Ferrari et al., 2003), and thermal management for electronic components (Pavlova & Amitay, 2006). When used for cooling, impinging jets can achieve high heat transfer rates compared with other common single-phase cooling methods such as parallel forced flow or natural convection (New & Yu, 2015). Confined impinging jets, in particular, are of interest for compact electronics packaging development (Garimella, 2000).

The flow field resulting from jet impingement consists of several regions that show distinct flow features (Carlomagno & Ianiro, 2014), as shown in Figure 1a. A free jet region forms as fluid exits the jet orifice in the confinement plate. The jet potential/inviscid core, where the velocity is relatively uniform, is surrounded by a free shear layer where the jet entrains the ambient fluid and slowly expands (Hollworth & Wilson, 1984). As the jet approaches the bottom plate, the flow decelerates in the vertical direction and accelerates in the radial direction near the stagnation point. This acceleration in the radial direction forms a wall jet along the bottom wall of the confinement gap.

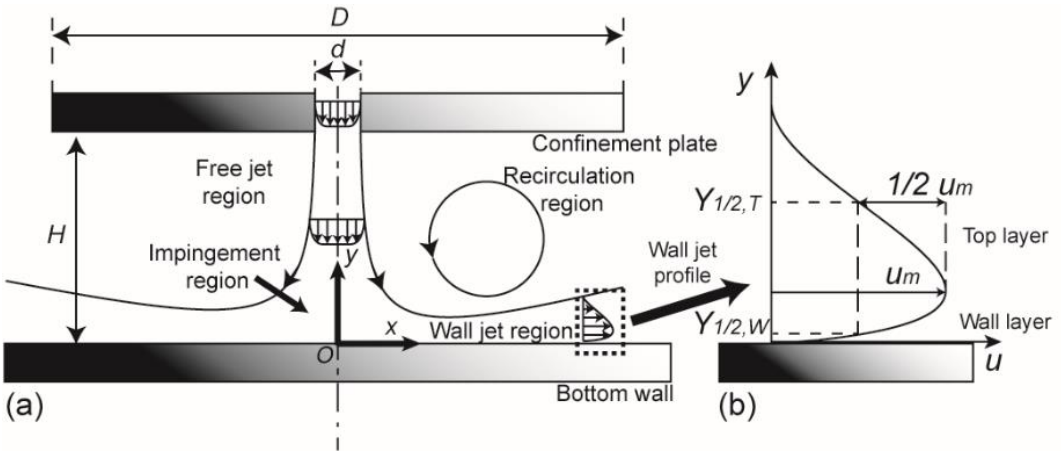

Figure 1. Schematic drawings of (a) the axisymmetric flow field formed by the impinging jet and, (b) the wall jet structure and nomenclature.

Wall jets are characterized by a triple-layered structure, as shown in Figure 1b. The first detailed study of a wall jet was performed by Glauert (1956) in his pioneering work on the theoretical solutions of the boundary layer equation for a jet spreading over a plane surface (Glauert, 1956). A self-similar solution would require the local maximum velocity (u_m) and wall jet half-width ($Y_{1/2,i}$) to be functions of the radial downstream location x/d in the form of

$$\frac{u_m}{V_j} \propto \left(\frac{x}{d}\right)^{\alpha}, \tag{1}$$

$$\frac{Y_{1/2,i}}{d} \propto \left(\frac{x}{d}\right)^{\beta_i}, \tag{2}$$

where the exponent α is referred to as the decay rate of u_m, and β_i is the growth rate of $Y_{1/2,i}$. Here, $i = T,W$ indicates the top layer or wall layer, respectively. The wall jet is subject to an incomplete self-similarity as the inner and outer regions of the flow scale differently, based on the triple-layer hypothesis proposed by Barenblatt for planar wall jets

(Barenblatt et al., 2005). The values of α, β_i and C_i are determined by performing a linear fit to experimental data plotted on a bi-logarithmic scale. The resulting expression for the nominal jet half-width $y_{1/2,i}$ is given by

$$\frac{y_{1/2,i}}{d} = e^{C_i}\left(\frac{x}{d}\right)^{\beta_i}. \tag{3}$$

In the case of a confined impinging jet with small confinement gaps, a recirculation region also exists where the flow is driven by both the free jet and the wall jet (Fitzgerald & Garimella, 1997, 1998). The flow rotates at a relatively low velocity, forming a stable toroidal vortex structure, as depicted in Figure 1a. This recirculation region represents a secondary motion induced by the impinging and wall jets and has been shown to enhance the heat exchange process at radial distances between x/d = 1.5 and 4 due to the reattachment of the recirculating liquid with the bottom wall (Garimella & Rice, 1995).

Although the flow field created by the impinging jet has attracted numerous research efforts for both heat transfer and fluid dynamics applications, many questions remain unanswered: not much attention in the literature has been paid to the wall jet development in a confined geometry. The main focus of the current study is to provide a detailed experimental investigation of the influence of the confinement on the flow field and radial wall jet development. Special attention has been given to the effect of the recirculation structure on the early development of the wall jet and the notion of incomplete self-similarity is tested. To the authors' best knowledge, this is the first experimental work on the effect of the confinement on the self-similar structure of a radial wall jet.

1.2 Experimental Method

1.2.1 Test section

A detailed description of the experimental facility was given by (Rau & Garimella, 2013). Only necessary details of the facility and SPIV measurement system have been included here for brevity. A schematic drawing of the test section is shown in Figure 2. The jet was formed by a round, sharp-edged orifice 3.75 mm in diameter (d) and two diameters in length. The orifice was located at the center of the upper confinement plate. Precision-machined stainless steel pins defined the nozzle-to-plate spacings (L)/confinement heights (H) between the confinement plate and bottom wall. A 25.4 mm diameter (6.7d) circular copper surface was flush-mounted in the bottom of the confinement gap bottom wall. This copper portion, with its center aligned with the jet axis, was used for the heat transfer studies of (Rau et al., 2016). No heat input was used during the current study. A small gap around the perimeter of the copper surface (on the order of 100 μm) is found to cause a slight disruption in the inner layer of the wall jet at Reynolds numbers greater than 1,000. The diameter (D) of the upper confinement plate was 70 mm, resulting in a confinement gap that extended 9.3 jet diameters downstream from the jet axis.

Two high-speed cameras (Phantom Miro M340, Vision Research) were installed with viewing angles of 35° and 10°, as shown in Figure 2. Lens tilt adapters were used to satisfy the Scheimpflug condition for SPIV (Willert, 1997). While the polycarbonate front and back walls of the test section were transparent and allowed full optical access, the side walls were made from opaque polyether-ether ketone (PEEK). The 2 mm thick laser sheet was introduced to the test section through the back wall and reflected across the

axisymmetric plane of interest with a mirror mounted inside the test section, as shown in Figure 2.

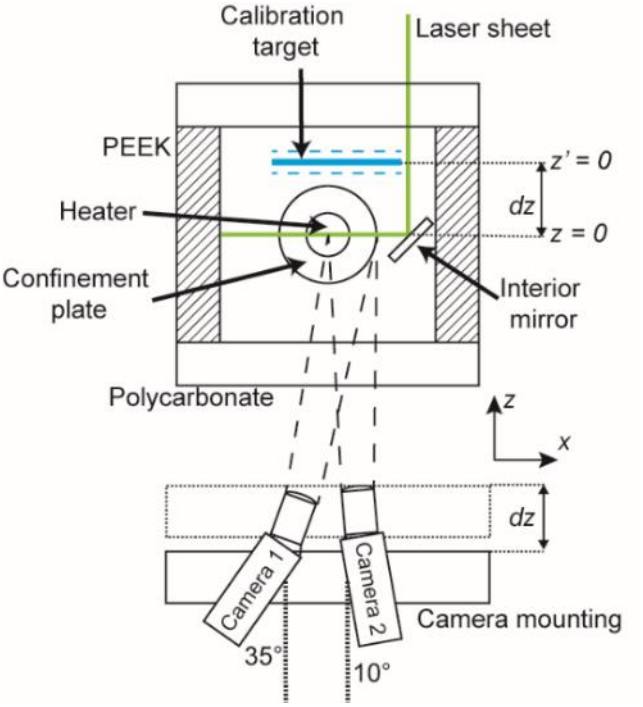

Figure 2. A schematic drawing showing a top view of the test section and camera positions for data recording and camera calibration.

1.2.2 Data recording

Five Reynolds numbers ranging from 1,000 to 9,000 at confinement heights of H/d = 2, 4 and 8 were investigated, as listed in Table 1. The double pulses from the laser (Nd:YLF Terra PIV 527-80-M, Continuum, 527 nm) were synchronized with the cameras recording single image exposures at an image pair frequency of 750 Hz. The liquid flow rate was obtained by an in-line Coriolis flow meter (CMFS015M, Emerson).

Fluorescent polystyrene microspheres of 10 μm in diameter (Spherotech) were used as seeding particles. The seeding density was maintained at a minimum of 10 particles per 32 × 32 pixel window by periodic re-seeding. This ensured sufficient mutual information

between sequential images for meaningful cross-correlation with low measurement uncertainty (Westerweel, 1994; Xue et al., 2015).

Table 1. Test matrix with jet velocity and time delay between laser pulses.

Re	H/d	V_j/(m/s)	Δt/ μs
1,000	2, 4, 8	0.24	1000
2,500	2, 4, 8	0.60	460
5,000	2, 4, 8	1.21	350
7,500	2, 4, 8	1.79	220
9,000	2, 4, 8	2.08	180

1.2.3 Camera calibration

Camera calibration to map the image coordinates to the world coordinates were obtained by calibrating each camera against a single-layer transparent glass target (FA131, Max Levy Autograph). The calibration followed the procedure by Prasad (Prasad, 2000). For calibration, the cameras and the target were translated a distance *dz* so that the calibration target could move unobstructed by the inner mirror, as shown in Figure 2. Calibration images were recorded at 7 planes from z' = -1.5mm to z' = 1.5mm with a 0.5 mm increment and were used to construct the calibration mapping functions. Self-calibration was then performed (Wieneke, 2005). The final mapping functions were applied in the three-component velocity reconstruction using the two-dimensional, two-component vector field from each camera based on the generalized reconstruction procedure (Soloff et al., 1999).

1.2.4 Data processing

Prior to PIV evaluations, the images were pre-processed to eliminate background noise. A local minimum subtraction was applied at each pixel across the entire time series for each test case. An in-house PIV code, Prana for stereo-PIV (https://github.com/aether-

lab/prana) implemented in Matlab (Mathworks) was used to perform the PIV evaluation and stereo reconstruction. Cross-correlation between frames was performed using the robust phase correlation (RPC) (Eckstein & Vlachos, 2009a, 2009b; Eckstein et al., 2008). RPC substantially reduces bias errors and peak-locking effects in the presence of high shear and rotational motion in comparison with standard cross-correlation algorithms. In addition, the time-averaged velocity field was obtained with an ensemble correlation scheme (Delnoij et al., 1999) using 1000 correlation planes for each case.

For the overall flow field velocity evaluation, a 64 × 64 ($x \times y$) pixel square-windowed interrogation region was used for the first pass, reduced to a 32 × 32 pixel window for the subsequent passes. A 75% window overlap delivered a final spatial vector resolution of 200 μm in the x and y direction. A different set of PIV evaluation parameters were used to resolve the thin wall jet. After the initial pass with a 64 × 64 pixel window, a window size of 64 × 4 pixels was used for a spatial resolution of 25 μm in the y direction. Using ensemble correlation in order to increase the correlation strength enabled this narrow window size, similar to the approach used by Westerweel (Westerweel et al., 2004).

For all PIV evaluations, a continuous window offset with iterative window deformation (Scarano, 2001) was applied to compensate for in-plane velocity gradients. The first and intermediate passes were followed by vector validation, using universal outlier detection (UOD) (Westerweel & Scarano, 2005) to remove and replace spurious vectors, and a Gaussian smoothing filter. No smoothing was applied after the final pass.

1.3 Results

1.3.1 Recirculation pattern

The flow field within the confinement gap consists of several distinct flow regions as described in the introduction. Similar to the flow visualization results reported by Garimella and colleagues (Fitzgerald & Garimella, 1997, 1998; Garimella & Rice, 1995), a recirculation pattern is observed in the current study. Streamtraces obtained from the ensemble-averaged flow field are overlaid on top of contours of normalized velocity magnitude as shown in Figure 3. In-plane velocity vectors are plotted in the regions of the vertical jet and wall jet. At Re = 1,000, counter-clockwise recirculation zones are observed at H/d = 2 and H/d = 4, though no recirculation is evident at H/d = 8. At Re = 9000, this counter-clockwise recirculation is observed for the most confined case at H/d = 2, but is no longer present at H/d = 4. At this Re = 9,000, a clockwise recirculation occurs at H/d = 8, but with a much lower velocity compared to the recirculation at H/d = 2 for this Reynolds number.

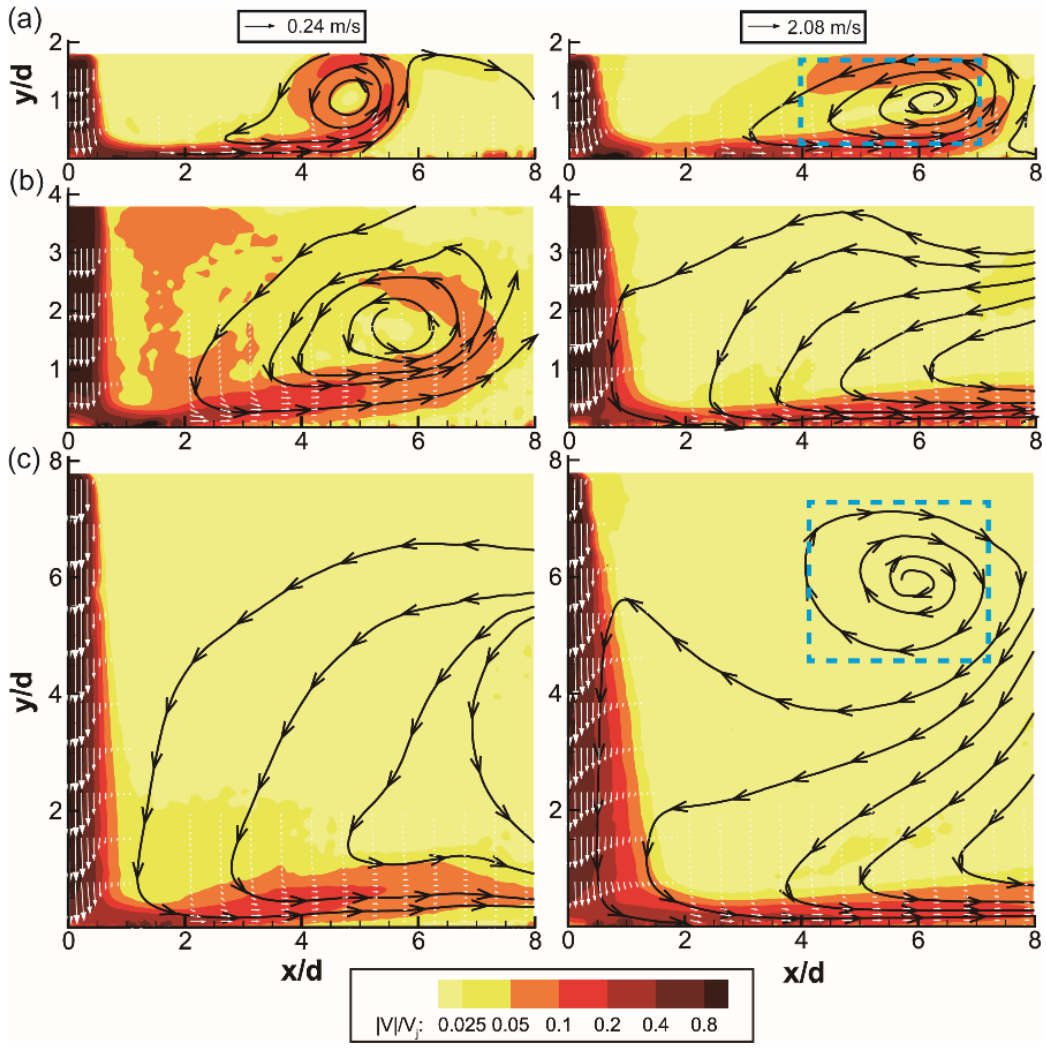

Figure 3. Streamtraces overlaid on contours of velocity magnitude for Re = 1000 in the left column and Re = 9000 in the right column, at confinement heights of (a) H/d = 2, (b) H/d = 4 and, (c) H/d = 8. Velocity vectors are plotted within the impinging jet and wall jet regions.

1.3.2 Decay rate of the local maximum velocity (u_m)

The local maximum radial-velocity component (u_m) as a function of downstream location from the jet centerline (x/d) for Re = 1,000-9,000 is plotted with a bi-logarithmic scale in Figure 4 for the confinement heights of H/d = 2, H/d = 4, and H/d = 8. At H/d = 8 (Figure 4c), the linear decay of u_m begins at x/d = 2.72 ($\ln(x/d)$ = 1.0) and continues beyond x/d = 8, out of the measurement domain. A similar region of linear decay occurs at x/d = 2.1 for H/d = 4 (Figure 4b), with the linear region again extending past the measurement domain. However, at H/d = 2 (Figure 4a), the region of linear decay of u_m ends within the range of the present flow field measurements. The end of this linear region moves further downstream from the jet centerline as Reynolds number increases, extending from x/d = 4.5 ($\ln(x/d)$ = 1.5) at Re = 2,500 to x/d = 6 ($\ln(x/d)$ = 1.8) at Re = 9,000, indicating a dependence on the jet momentum. A critical distance for the decay rate ($l_{crit,\alpha}$) is defined as the length from the jet centerline to the cessation location of the linear decay region of u_m, which is determined as the location where a sudden increase in the magnitude of the velocity decay occurs. The critical velocity (u_{crit}) is defined as the corresponding u_m for each Reynolds number at $l_{crit,\alpha}$, normalized by the jet velocity (V_j). Interestingly, while the $l_{crit,\alpha}$ changes with jet Reynolds number, the u_{crit} for all Reynolds numbers are the same and equal to u_m/V_j = 0.15 ($\ln(u_m/V_j)$=-1.9).

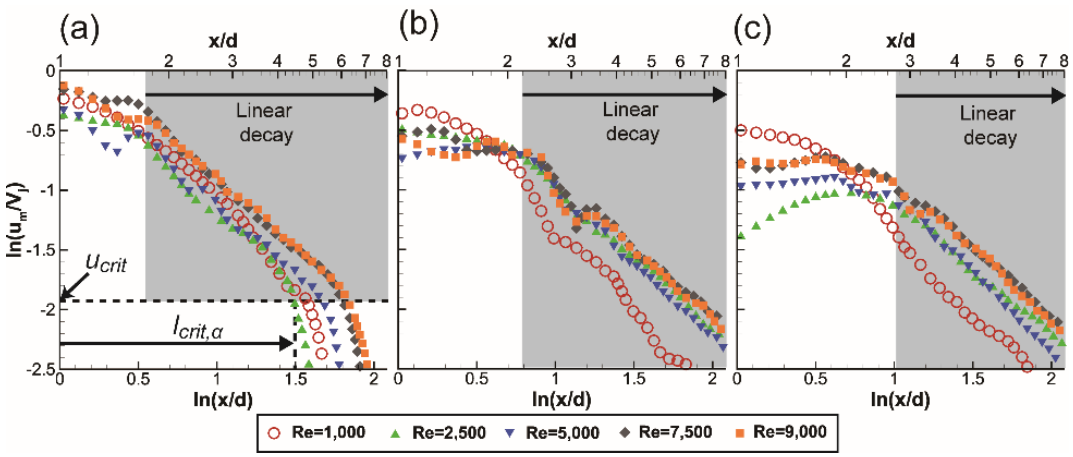

Figure 4. Decay of u_m for the confinement heights of (a) H/d = 2, (b) H/d = 4 and (c) H/d = 8 for the range from x/d = 1 to x/d = 8. The shaded areas indicate the linear decay range. The dashed line in (a) indicates the u_{crit} and the $l_{crit,\alpha}$ for Re = 2,500 is shown as an example.

A velocity decay rate is calculated by fitting an equation of the form of Equation (1) to the linear regions shown in Figure 4. The resulting decay rate (α) for each case is plotted in Figure 5. Representative results from the literature (Bakke, 1957; Knowles & Myszko, 1998; Loureiro & Freire, 2012; Poreh et al., 1967; Tanaka & Tanaka, 1977) for radial wall jets are tabulated in Table 2 for comparison with their range also denoted by the shaded area in the Figure 5. As is shown in the figure, the values for α at Re = 1,000 differ from the literature, indicating a faster decay of wall jet velocity at this low Reynolds number. The decay rate for the higher Reynolds numbers (Re = 2,500, 5,000, 7,500, and 9,000) show good agreement with previous studies including: jets with and without confinement, nozzle-to-plate distances (L/d) ranging from 0.5282 to 25, and Reynolds numbers ranging from 2,500 to 288,000.

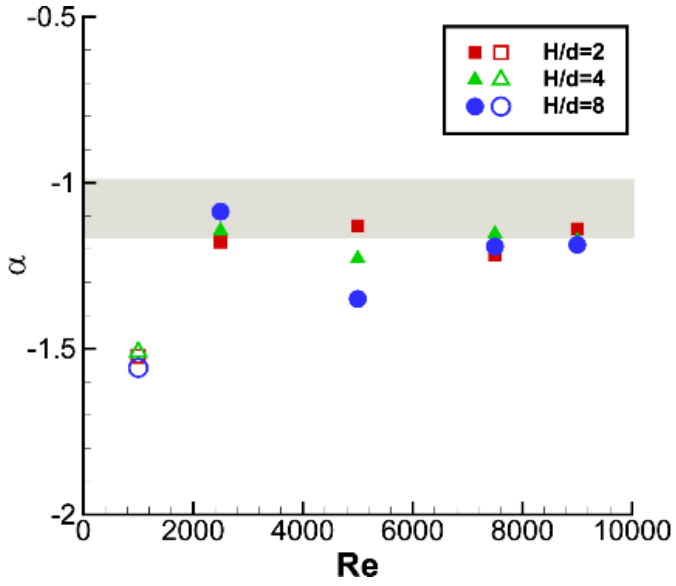

Figure 5. Decay rate of u_m as a function of both Reynolds number and confinement height H/d. The shaded area indicates the range of values from the literature listed in Table 2.

Table 2. Decay rate of u_m for radial wall jets from the literature.

	L/d	*x/d* range	Re	α	Confinement
Bakke (1957)	0.5282	5~10	3.5 k	-1.12	No
Poreh *et al.* (1967)	6.6, 9.85, 19.7	10~60	107 k~ 288 k	-1.1	No
Tanaka (1977)	N/A	2~100	7.5 k~ 55 k	-1.09	No
Knowles (1998)	2,4,8,10	1~10	90 k	-1.168	No
Loureiro (2012)	2	1~5	47 k	-0.989	Yes

1.3.3 Jet core length (l_c) and turbulent kinetic energy in the vertical jet

The difference in the decay rates of the wall jet between Re = 1,000 cases and all other cases may arise due to a difference in the characteristics of the vertical impinging jet at this low Reynolds number. We investigated this difference by looking at the jet core length and turbulent kinetic energy. The jet core length (l_c) is defined as the distance from the jet orifice to the point where the centerline velocity has decayed to 95% of V_j. Figure 6 shows l_c normalized by the corresponding confinement heights (H) for all test cases. For Re = 1,000, the jet core is able to extend almost 85% of the entire gap at confinement height of H/d = 8 before the jet impinges on the bottom plate. As the Reynolds number increases, the jet core length at H/d = 8 drops by 68% at Re = 2,500 compared with the value at Re = 1,000, then recovers and stabilizes at about 55% of the length at Re = 1,000, implying a fully developed regime at higher Reynolds number after a transition at Re =2,500. For Re =1,000 cases, the bottom plate forces the impinging jet vertical velocity to decay much faster if compared with non-impinging free jets at the same Reynolds number. While for higher Reynolds number cases, this forced deceleration is less pronounced due to the fact that the core length of the non-impinging free jets is by nature shorter due to the growing shear layer and increased turbulent kinetic energies.

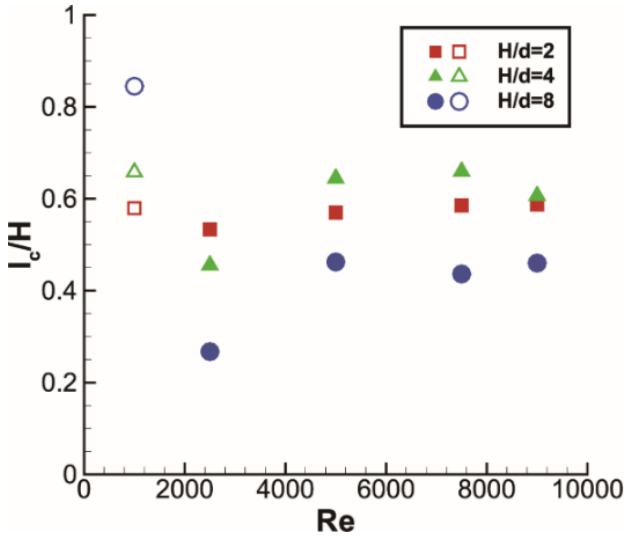

Figure 6. The jet core length normalized by the confinement heights as a function of jet Reynolds number.

To further investigate the turbulence characteristics of the impinging jets, turbulence kinetic energies (TKE) are calculated for Re = 1,000, 2,500, and 5,000 for the three confinement heights and plotted in Figure 7. TKE is calculated using *u*, *v*, *w* velocity fluctuations obtained from 1000 time instances and non-dimensionalized by the squared jet velocity (V_j^2). For Re = 1,000, TKE is only significant in the thin shear layer surrounding the vertical jet and the wall layer after impingement, with TKE values in this region being greater than 0.1. At this low Reynolds number, TKE along the centerline of the jet remains very low in magnitude (with a magnitude of less than 0.1), with turbulence from the shear layer only reaching the jet centerline for H/d = 8 near the impingement surface at $y/d \approx 2.2$. This low turbulence at the center of the jet suggests an extended laminar potential core region, which would help preserve vertical jet momentum before impingement. On the contrary, centerline turbulence is much higher for the Re = 2,500 and 5,000 cases, suggesting a shorter jet potential core and reduced impingement momentum. The initial conditions for the developing wall jet at the higher Reynolds

numbers in this study, thus, have higher levels of turbulence and reduced momentum compared to the Re = 1,000 case.

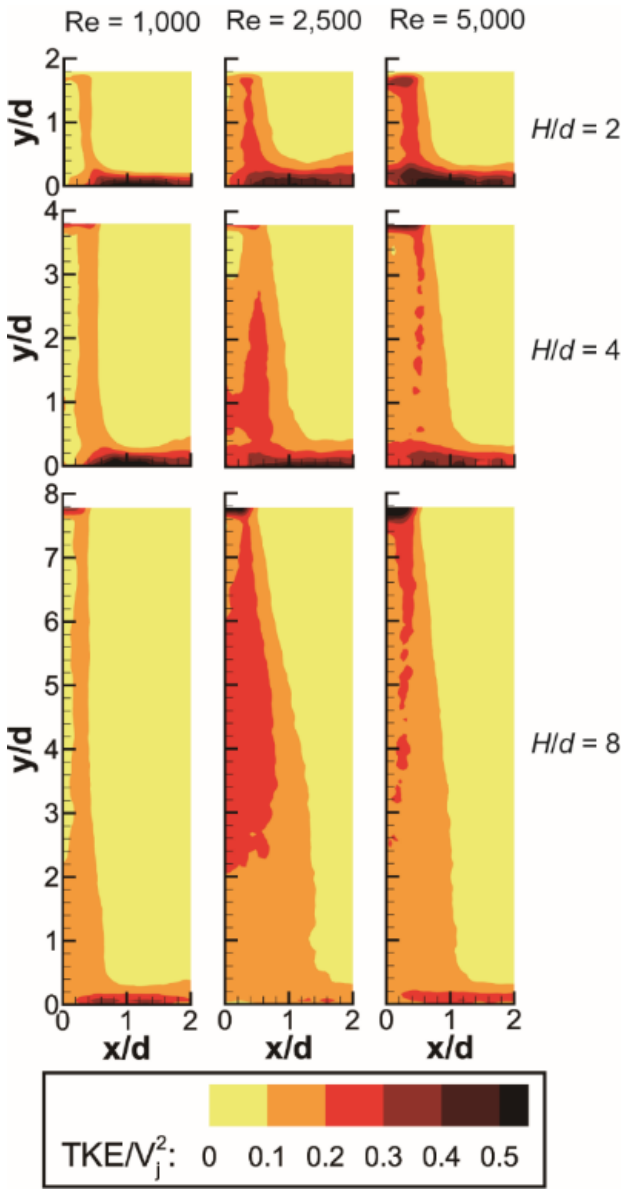

Figure 7. Dimensionless turbulence kinetic energy contours for Re = 1,000, 2,500 and 5,000 at *H*/*d* = 2, 4 and 8.

1.3.4 Growth rate of the wall jet thickness $Y_{1/2,i}$

Due to this small gap between the heater and the bottom plate as introduced in Section 1.2.1, the wall layer half-width development is not properly resolved at higher Reynolds numbers in the current study. To be conservative and consistent, only the growth rates for the Re = 1,000 cases are presented for discussion. The upper and lower $Y_{1/2}$ are plotted with a bi-logarithmic scale for different confinement heights at Re = 1,000 in Figure 8. The exact values for $Y_{1/2,T}$ and $Y_{1/2,W}$ are determined by spline interpolation to determine the precise y/d position where $u/u_m = 1/2$ occurs at each x/d location. The range used for linear fitting and scaling analysis is shown with the solid lines overlaid on the plotted data in Figure 8. Data are included in the linear fit if they fall within the linear decay range of u_m (as shown in Figure 4) and only regions where data for the top layer and wall layer overlap are considered in the comparison. As shown with the lines in Figure 8, the x/d range where the linear growth occurs moves further downstream as the confinement height increases.

The growth rates resulting from the fit of Equation (2) to the data shown in Figure 8 are listed in Table 3 as the shaded rows. As the confinement height is reduced, the growth rate of the wall jet increases from $\beta_T = 0.889$ at $H/d = 8$ to $\beta_T = 1.340$ at $H/d = 4$. The growth rate of the inner layer also increases from $\beta_W = 0.868$ at $H/d = 8$ to $\beta_W = 1.746$ at $H/d = 2$. The results show that the growth of the boundary layer accelerates as the confinement height is reduced.

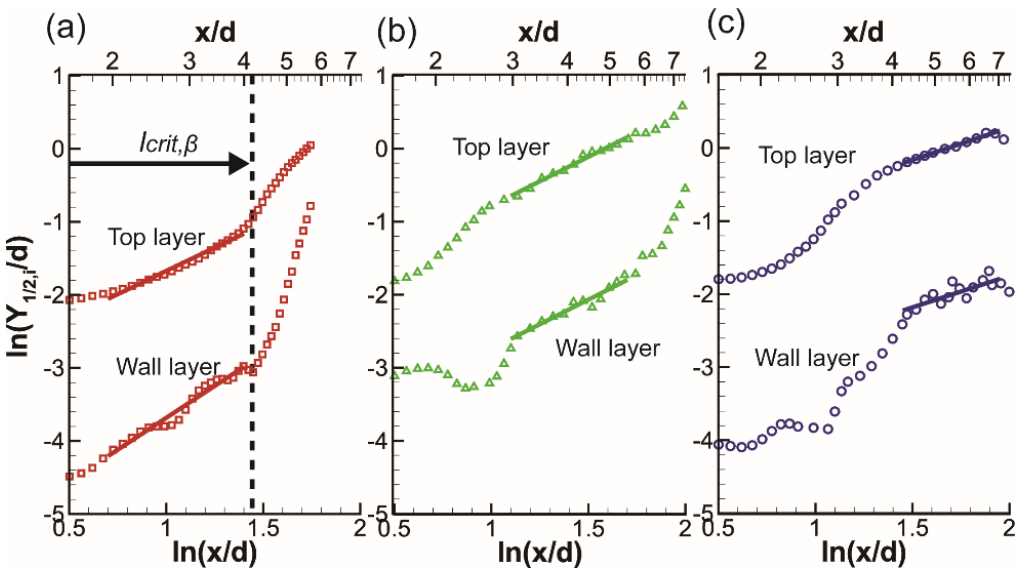

Figure 8. The $Y_{1/2,T}$ and $Y_{1/2,W}$ for different (a) H/d = 2, (b) H/d = 4, and (c) H/d = 8 at Re = 1,000. The solid lines indicate the linear growth range that is used for scaling analysis. The dashed line corresponds to the critical distance for the linear growth of wall jet half-widths.

Values for β_i from previous studies in the literature (Bakke, 1957; Barenblatt et al., 2005; Knowles & Myszko, 1998; Poreh et al., 1967; Tanaka & Tanaka, 1977; Tang et al., 2015) are also tabulated in Table 3 for comparison. The current results show that for Re = 1,000 at H/d = 4 and 8, there is little difference between β_i for the top layer and wall layer. This is not in agreement with the incomplete self-similarity proposed by Barenblatt *et al.* (2005). In contrast, a large difference is observed for β_i in the top and bottom layers at H/d = 2, indicating that the incomplete self-similarity occurs at this confinement gap height. Results at additional confinement gap heights and Reynolds numbers are needed to verify whether this self-similarity is universally maintained at higher confinement spacings.

Table 3. Growth rate for both top and wall layers for Re = 1,000 cases and from literature.

	Type	x/d range	Surface	Re	β_T	β_W
$H/d = 2$	Radial	2.0~4.0	Smooth	1,000	1.275	1.746
$H/d = 4$	Radial	3.0~5.5	Smooth	1,000	1.340	1.347
$H/d = 8$	Radial	4.1~6.7	Smooth	1,000	0.889	0.868
Bakke (1957)	Radial	5~10	Smooth	3,500	0.94	N/A
Poreh *et al.* (1967)	Radial	10~60	Smooth	107,000~288,000	0.9	N/A
Tanaka & Tanaka (1977)	Radial	2~100	Smooth	7,500~55,000	0.97	N/A
Knowles & Myszko (1998)	Radial	1~10	Smooth	90,000	1	N/A
Barenblatt *et al.* (2005)	Planar	40~150	Smooth	9,600	0.93	0.68
Tang *et al.* (2015)	Planar	30~80	Smooth	7,500	0.780	0.504
Tang *et al.* (2015)	Planar	30~80	Rough	7,500	0.817	0.403

1.3.5 Self-similarity of the velocity profile in the wall jet at Re = 1,000

The self-similarity of the velocity profiles is further investigated using the fitted coefficients β_i for both the top layer and the wall layer. The velocity magnitude is normalized by u_m at each x/d location and the vertical distance from the bottom wall is non-dimensionalized by the nominal $y_{1/2,i}$, given by Equation (3), using the coefficients from the fitting results. The rescaled velocity profiles, shown in Figure 9, are plotted in the range where the linear growth of the wall jet holds, as discussed in Section 1.3.4.

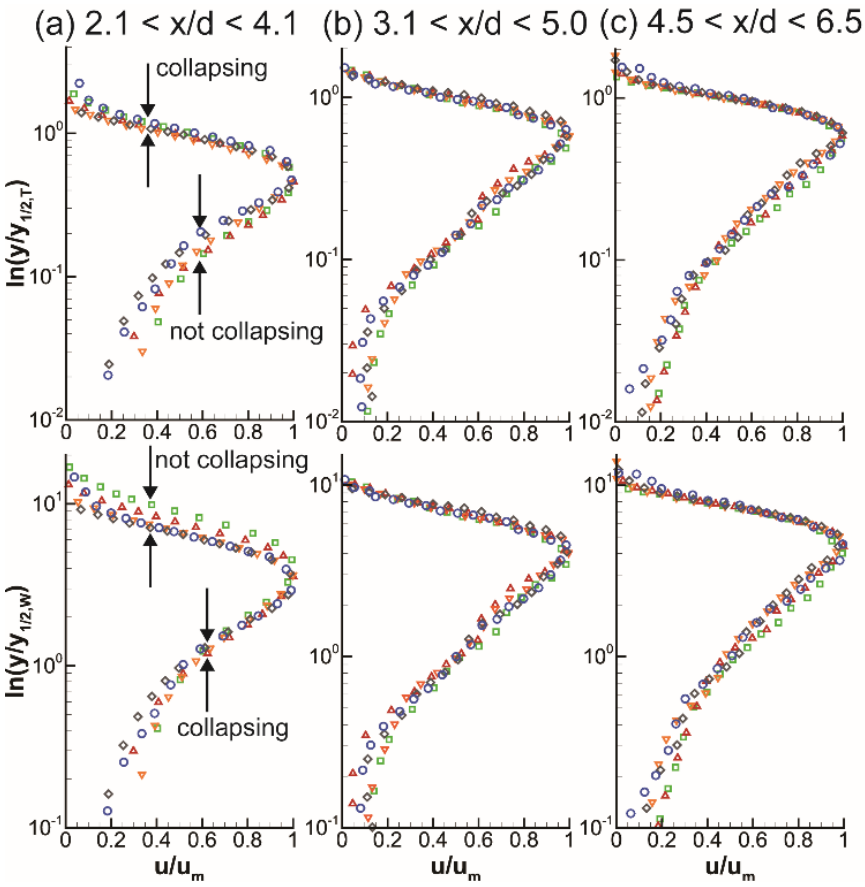

Figure 9. Velocity profile collapse for Re = 1,000 for (a) H/d = 2, (b) H/d = 4 and (c) H/d = 8. Data in the top row are plotted with vertical distance (y) non-dimensionalized by $y_{1/2,T}$,while data in the bottom row are plotted with vertical distance (y) non-dimensionalized by $y_{1/2,W}$. Velocities are normalized by the local u_m.

As shown in Figure 9, no major difference is observed between the velocity profiles scaled with the top layer coefficients and wall layer coefficients for $H/d = 4$ and $H/d = 8$. This result is expected given the small differences in β_T and β_W that determined for at $H/d = 4$ and $H/d = 8$. The velocity profiles for these cases do not display the incomplete self-similarity proposed by Barenblatt *et al*. (2005), and also show that self-similarity coincides within the linear growth range of $Y_{1/2,i}$. In contrast, the velocity profiles for $H/d = 2$ shown in Figure 9 do display incomplete self-similarity. Only the top of the velocity profile collapses when normalized with β_T, while only the inner layer of the profile collapses when normalized with β_W.

1.3.6 Recirculation structure and swirling strength

Time-averaged vortical structures are identified using λ_{ci} criterion proposed by Zhou (Zhou et al., 1999), where the imaginary part of the complex eigenvalue of the velocity gradient tensor (λ_{ci}) is calculated and referred to as the local swirling strength of the vortex. Contours of swirling strength are plotted in Figure 10 for the regions of the flow shown with the dashed windows in Figure 3. Note that the vertical range of the plot for the H/d = 8 case is different from the H/d = 2 cases.

As shown in Figure 10 a to c for H/d = 2, the recirculation core moves outwards away from the jet with increasing Reynolds number. This outward movement is accompanied by a decrease in the magnitude of the swirling strength. Figure 10d shows a recirculation zone that occurs at H/d = 8. It can be observed that the swirling direction is opposite for this higher confinement gap spacing compared to the H/d = 2 cases shown in Figure 10. The reversed recirculation direction is a result of the distinctly different mechanism generating the liquid motion at the large confinement gap spacing. At the smallest confinement height, the motion caused by entrainment has a greater influence on the surrounding flow field due to the reduced cross-sectional area in the gap; a counter-clockwise rotation results as liquid in the wall jet recirculates back towards the vertical jet. In contrast, the recirculation at H/d = 8 occurs near the top edge of the confinement gap, as shown in Figure 3. This recirculation is formed due to the slow motion of surrounding liquid outside of the confinement gap being drawn into the confined space. Due to the lower liquid velocities inherent for this process, the resulting swirling strength of the vortex observed at H/d = 8 is lower compared to the intense recirculation observed at H/d = 2.

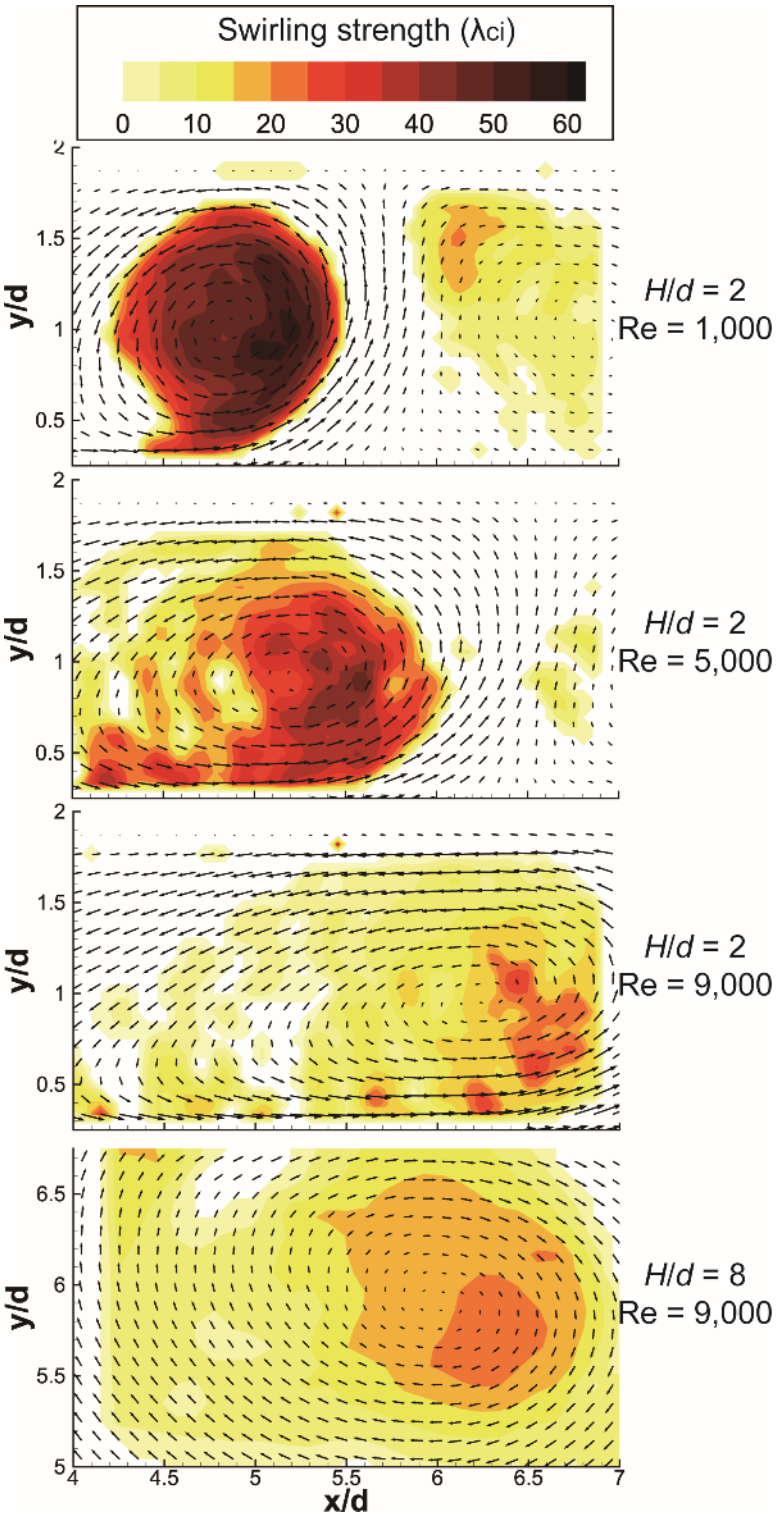

Figure 10. The recirculation core and contours of the swirling strength.

1.4 Discussion

Much of the information in the literature on wall jets has been obtained through the study of planar wall jets (Launder & Rodi, 1983). The evolution of the *length scales* of planar and radial wall jets, (*i.e*. the growth rate of the $Y_{1/2,i}$) are very close (Banyassady, 2015). Typical growth rates for both planar and radial wall jets are $\beta_T \approx 0.8\sim1$ (Bakke, 1957; Barenblatt et al., 2005; Knowles & Myszko, 1998; Poreh et al., 1967; Tanaka & Tanaka, 1977; Tang et al., 2015). However, the evolution of the *velocity scales* (i.*e*. the decay rate of the local u_m) is dependent on the wall jet geometry; the radial wall jet decelerates faster due to spreading in the azimuthal direction. Typical decay rates for planar wall jets range from $\alpha \approx$ -0.6 to -0.5 (Barenblatt et al., 2005; Tang et al., 2015), which is much lower than the typical values for radial wall jets ($\alpha \approx$ -1 to -1.2) (Bakke, 1957; Poreh et al., 1967). Thus, the decay rate of maximum velocity in this study is only compared to results from radial wall jets in the literature in Section 1.3.2, while results from both planar and radial studies are used for comparison of growth rate in Section 1.3.4. To the authors' best knowledge, little has been reported regarding the triple-layered incomplete self-similarity for radial wall jets, therefore comparison of this is limited to results obtained from planar wall jet studies.

The growth rate is much higher at $H/d = 2$ than at the larger confinement gap heights. At $H/d = 8$, the β_T and β_w values are 0.889 and 0.868, which are close to the values reported in the literature for unconfined wall jets. As the upper confinement plates moves closer to the bottom wall, the values of β_T and β_w increase to 1.340 and 1.347 at $H/d = 4$, and 1.275 and 1.746 at $H/d = 2$. This trend indicates that smaller confinement gap heights increase the growth of the boundary layer on the bottom plate.

Confinement is not shown to have a large effect on the decay rate of u_m in the current study. For Reynolds numbers above 2,500, the decay rate has a universal value $\alpha \approx$ -1.1 to -1.2, regardless of confinement heights. Furthermore, the velocity profiles at H/d = 2 are found to not reach self-similarity, indicating that the overall decay of radial velocity is negligibly influenced by the self-similarity of the wall jet. Given these results, it is apparent that confinement does not have a strong influence on the decay rate of u_m, but it does alter self-similarity and the range where the linear growth occurs, as shown in Figure 8.

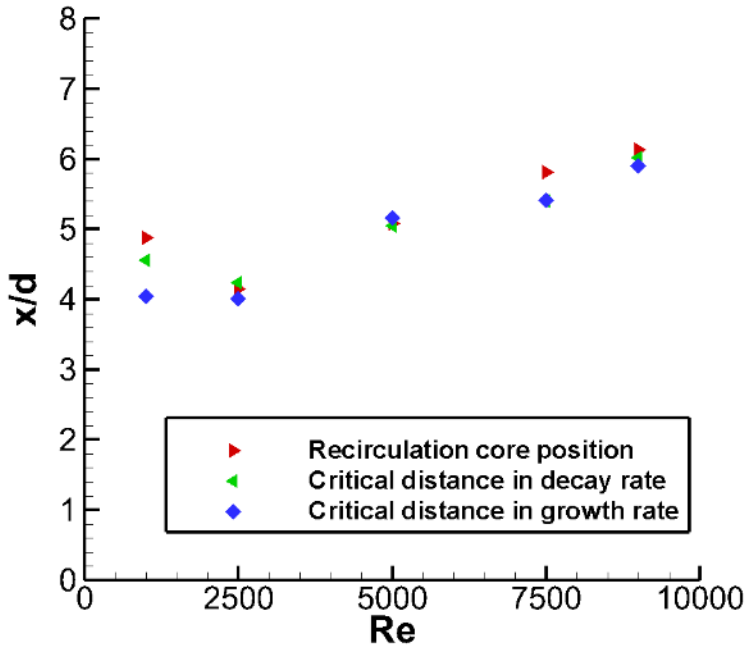

Figure 11. The radial position of the recirculation core plotted with the critical distance in linear decay of u_m and critical distance in the linear growth of $Y_{1/2,i}$ for H/d = 2 as a function of Reynolds number.

The critical distance for the decay and growth rate ($l_{crit,\alpha}$ and $l_{crit,\beta}$ shown in Figure 4a and Figure 8a) indicates where the end of the linear decay of u_m and linear growth of $Y_{1/2,i}$ occurs at H/d = 2. The critical distances as a function of Reynolds number are plotted in

Figure 11 together with the recirculation core position as shown in Figure 10. For the same Reynolds number, the radial position of the recirculation core and the critical distances for growth rate and decay rate lie within 1 jet diameter of each other. This suggests that the early termination of the linear decay and growth region is caused by the recirculation of liquid within the gap at $H/d = 2$. Boundary layer separation is caused by the axisymmetric vortex ring, which interrupts the development of the wall jet. The wall jet velocity decays exponentially until a critical value of maximum radial velocity (u_{crit}) is reached, after which the radial momentum is weak enough to be overcome by the recirculation. The critical velocity is found to be $u_{crit}/V_j = 0.15$ for all $H/d = 2$ cases studied.

CHAPTER 2. CONCLUSION REMARKS

2.1 Summary of the Current Work

The current study fills in the research blank of the radial wall-jet development in the near field downstream of the impingement in the confined space. The confinement has been found to significantly alter both the overall flow regime, the free-jet development and the wall-jet development.

The decay rate of the local maximum velocity in the wall-jet region is found to have a universal constant close to -1.1 in the developing region, which is close to the decay rate reported by other researchers for the fully-developed region for radial wall-jets. The related hypothesis would be that the development of the self-similarity only re-distributes the momentum flux along the vertical direction, and the momentum flux strength decays regardless of the velocity profile. And the confinement is found not to affect this process. At low Re, which is 1,000 in the current study, the decay rate of the local maximum velocity in the wall-jet region is much higher than other cases investigated. This might be due to the starting vertical jet still lies in the laminar regime.

Contrary to what Barenblatt proposed, no major difference has been found regarding the rate of growth for the top and wall layers of the wall-jet, at low Re regime in the early stage of the wall-jet development at H/d=4 and 8 confinement heights. Velocity profile collapsing using top and wall layer scaling constants respectively is shown for Re=1,000

according to the triple-layered in-complete self-similarity proposed by Barenblatt, but only the H/d=2 case shows difference due to the discrepancy in β^i .

The confinement height has been found to influence the free-jet region before impingement and make a difference in the starting condition for the wall-jet region to start developing with. The H/d=2 confinement height cases have a more uniform potential core length across the Re and a larger expansion angle compared to the other confinement heights. As a result, the H/d=2 cases show much higher mass entrainment coefficients than the less confined cases. The confinement height has also been found to alter the direction of recirculation. The donut-like rotating motion of the ambient liquid is found to be counter-clockwise for H/d=2 cases and clockwise for H/d=8 cases. And the recirculation cores for the H/d=2 cases are proven to locate where the transition points of the rate of decay curve and rate of growth curve are, in terms of downstream location x/d.

2.2 Limitation of the Current Work and Future Work

The main constrain of the current work is due to the disturbance caused by the heater edge, which prevents the analysis of inner layer scaling for higher Reynolds number cases. Also a higher spatial resolution could be achieved if the cameras are only looking at the wall-jet region, which will give more vectors in the wall layer for better interpolation and scaling analysis. Additionally, the overall flow pattern could have been better analyzed using the adaptive windowing PIV scheme (Theunissen et al., 2006), which may aid in improving the spatial resolution by locally optimization of the interrogation window.

A fixed sampling rate of 750 Hz is used for all the Re cases, which limits the temporal resolution of the measurement, preventing further analysis of the turbulent intensity and coherent structure from the instantaneous flow field. To better capture the flow dynamics

in the low-velocity region, a multi-frame PIV evaluation scheme (Persoons & O'Donovan, 2008) could be used to enhance the measurement dynamic range.

A simultaneous local heat transfer measurement together with PIV measurement can be used to look into the coherent structure evolvement and the well-known secondary annular peak of Nusselt number (Gardon, 1962).

LIST OF REFERENCES

LIST OF REFERENCES

1. Bakke, P. (1957). An experimental investigation of a wall jet. *Journal of Fluid Mechanics*, *2*(05), 467. http://doi.org/10.1017/S0022112057000270

2. Banyassady, R. (2015). *Large-eddy simulations of plane and radial wall-jets over smooth and rough surfaces*.

3. Barenblatt, G. I., Chorin, A J., & Prostokishin, V. M. (2005). The turbulent wall jet: a triple-layered structure and incomplete similarity. *Proceedings of the National Academy of Sciences of the United States of America*, *102*(25), 8850–8853. http://doi.org/10.1073/pnas.0503186102

4. Carlomagno, G. M., & Ianiro, A. (2014). Thermo-fluid-dynamics of submerged jets impinging at short nozzle-to-plate distance: A review. *Experimental Thermal and Fluid Science*, *58*, 15–35. http://doi.org/10.1016/j.expthermflusci.2014.06.010

5. Delnoij, E., Westerweel, J., Deen, N. G., Kuipers, J. A. M., & van Swaaij, W. P. M. (1999). Ensemble correlation PIV applied to bubble plumes rising in a bubble column. *Chemical Engineering Science*, *54*(21), 5159–5171. http://doi.org/10.1016/S0009-2509(99)00233-X

6. Eckstein, A., Charonko, J., & Vlachos, P. (2008). Phase correlation processing for DPIV measurements. *Experiments in Fluids*, *45*(3), 485–500. http://doi.org/10.1007/s00348-008-0492-6

7. Eckstein, A., & Vlachos, P. (2009a). Assessment of advanced windowing techniques for digital particle image velocimetry (DPIV). *Measurement Science and Technology*. Retrieved from http://iopscience.iop.org/0957-0233/20/7/075402

8. Eckstein, A., & Vlachos, P. (2009b). Digital particle image velocimetry (DPIV) robust phase correlation. *Measurement Science and Technology*, *20*(5), 055401. http://doi.org/10.1088/0957-0233/20/5/055401

9. Ferrari, J., Lior, N., & Slycke, J. (2003). An Evaluation of Gas Quenching of Steel Rings by Multiple-Jet Impingement. *Journal of Materials Processing Technology*, *136*(3), 190–201. http://doi.org/10.1016/S0924-0136(03)00158-4

10. Fitzgerald, J., & Garimella, S. (1997). Flow field effects on heat transfer in confined jet impingement. *Journal of Heat Transfer*, *119*(3), 630–632. http://doi.org/10.1115/1.2824152

11. Fitzgerald, J., & Garimella, S. (1998). A study of the flow field of a confined and submerged impinging jet. *International Journal of Heat and Mass Transfer*, *41*(8-9), 1025–1034. http://doi.org/10.1016/S0017-9310(97)00205-6

12. Gardon, R. (1962). Heat transfer between a flat plate and jets of air impinging on it. *Int. Dev. Heat Transfer (ASME)*, 454–460.

13. Garimella, S. V. (2000). HEAT TRANSFER AND FLOW FIELDS IN CONFINED JET IMPINGEMENT. Retrieved March 22, 2016, from http://www.dl.begellhouse.com/pt/references/5756967540dd1b03,58e189cd6ad96098,7cd26f8469f6a868.html

14. Garimella, S. V., & Rice, R. A. (1995). Confined and Submerged Liquid Jet Impingement Heat Transfer. *Journal of Heat Transfer*, *117*(4), 871. http://doi.org/10.1115/1.2836304

15. Glauert, M. B. (1956). The wall jet. *Journal of Fluid Mechanics*, *1*(06), 625–643. http://doi.org/10.1017/S002211205600041X

16. Han, J.-C. (2004). Recent Studies in Turbine Blade Cooling. *The International Journal of Rotating Machinery*, *10*(6), 443–457. http://doi.org/10.1080/10236210490503978

17. Hollworth, B. R., & Wilson, S. I. (1984). Entrapment effects on impingement heat transfer: Part I — Measurements of heated jet velocity and temperature distributions and recovery temperatures on target surface. *Journal of Heat Transfer*, *106*(November), 797–803.

18. Knowles, K., & Myszko, M. (1998). Turbulence measurements in radial wall-jets. *Experimental Thermal and Fluid Science*, *17*, 71–78. http://doi.org/10.1016/S0894-1777(97)10051-6

19. Launder, B. E., & Rodi, W. (1983). The turbulent wall jet -measurements and modeling. *Annual Review of Fluid Mechanics*.

20. Loureiro, J. B. R., & Freire, A. P. S. (2012). On the dynamic behaviour of turbulent impinging jets. *THMT-12. Proceedings of the Seventh International Symposium On Turbulence, Heat and Mass Transfer Palermo, Italy, 24-27*, 1–12.

21. New, D. T. H., & Yu, S. C. M. (2015). *Vortex Rings and Jets*. (D. T. H. New & S. C. M. Yu, Eds.). Springer.

22. Pavlova, A., & Amitay, M. (2006). Electronic Cooling Using Synthetic Jet Impingement. *Journal of Heat Transfer*, *128*(9), 897. http://doi.org/10.1115/1.2241889

23. Persoons, T., & O'Donovan, T. S. (2008). Improving the measurement accuracy of PIV in a synthetic jet flow. *14th International Symposium on Applications of Laser Techniques to Fluid Mechanics, Lisbon, Portugal, July 7-10, 2008*, 1044.

24. Poreh, M., Tsuei, Y. G., & Cermak, J. E. (1967). Investigation of a Turbulent Radial Wall Jet, 9–81.

25. Prasad, A. K. (2000). Stereoscopic particle image velocimetry. *Experiments in Fluids*, *29*(2), 103–116. http://doi.org/10.1007/s003480000143

26. Rau, M. J., & Garimella, S. V. (2013). Local two-phase heat transfer from arrays of confined and submerged impinging jets. *International Journal of Heat and Mass Transfer*, *67*, 487–498. http://doi.org/10.1016/j.ijheatmasstransfer.2013.08.041

27. Rau, M. J., Guo, T., Vlachos, P. P., & Garimella, S. V. (2016). Stereo-PIV Measurements of Vapor-Induced Flow Modifications in Confined Jet Impingement Boiling. *Submitted for Possible Publication in International Journal of Multiphase Flow*.

28. Sarkar, A., Nitin, N., Karwe, M. V., & Singh, R. P. (2004). Fluid Flow and Heat Transfer in Air Jet Impingement in Food Processing. *Journal of Food Science*, *69*(4), 113–122.

29. Scarano, F. (2001). Iterative image deformation methods in PIV. *Measurement Science and Technology*, *13*(1), R1–R19. http://doi.org/10.1088/0957-0233/13/1/201

30. Soloff, S. M., Adrian, R. J., & Liu, Z.-C. (1999). Distortion compensation for generalized stereoscopic particle image velocimetry. *Measurement Science and Technology*, *8*(12), 1441–1454. http://doi.org/10.1088/0957-0233/8/12/008

31. Tanaka, T., & Tanaka, E. (1977). Experimental studies of a radial turbulent jet. *Bulletin of the JSME*.

32. Tang, Z., Rostamy, N., Bergstrom, D. J., Bugg, J. D., & Sumner, D. (2015). Incomplete similarity of a plane turbulent wall jet on smooth and transitionally rough surfaces. *Journal of Turbulence*, *16*(11), 1076–1090. http://doi.org/10.1080/14685248.2015.1054034

33. Theunissen, R., Scarano, F., & Riethmuller, M. L. (2006). An adaptive sampling and windowing interrogation method in PIV. *Measurement Science and Technology*, *18*(1), 275–287. http://doi.org/10.1088/0957-0233/18/1/034

34. Westerweel, J. (1994). Efficient detection of spurious vectors in particle image velocimetry data. *Experiments in Fluids*, *272*(9), 263–272. http://doi.org/10.1007/bf00206543

35. Westerweel, J., Geelhoed, P. F., & Lindken, R. (2004). Single-pixel resolution ensemble correlation for micro-PIV applications. *Experiments in Fluids*, *37*(3), 375–384. http://doi.org/10.1007/s00348-004-0826-y

36. Westerweel, J., & Scarano, F. (2005). Universal outlier detection for PIV data. *Experiments in Fluids*, *39*(6), 1096–1100. http://doi.org/10.1007/s00348-005-0016-6

37. Wieneke, B. (2005). Stereo-PIV using self-calibration on particle images. *Experiments in Fluids*, *39*(2), 267–280. http://doi.org/10.1007/s00348-005-0962-z

38. Willert, C. (1997). Stereoscopic digital particle image velocimetry for application in wind tunnel flows. *Measurement Science and Technology*, *8*(12), 1465–1479. http://doi.org/10.1088/0957-0233/8/12/010

39. Xue, Z., Charonko, J. J., & Vlachos, P. P. (2015). Particle image pattern *mutual information* and uncertainty estimation for particle image velocimetry. *Measurement Science and Technology*, *26*(7), 074001. http://doi.org/10.1088/0957-0233/26/7/074001

40. Zhou, J., Adrian, R. J., Balachandar, S., & Kendall, T. M. (1999). Mechanisms for generating coherent packets of hairpin vortices in channel flow. *Journal of Fluid Mechanics*, *387*, 353–396. http://doi.org/10.1017/S002211209900467X